IEEE Access
Multidisciplinary | Rapid Review | Open Access Journal

Received June 7, 2019, accepted June 21, 2019, date of publication July 3, 2019, date of current version August 12, 2019.

Digital Object Identifier 10.1109/ACCESS.2019.2926809

Polarization Reconfigurable Air-Filled Substrate Integrated Waveguide Cavity-Backed Slot Antenna

KAMIL YAVUZ KAPUSUZ[1], (Student Member, IEEE), SAM LEMEY[1], (Member, IEEE), ALESSANDRA PETROCCHI[2], (Student Member, IEEE), PIET DEMEESTER[1], (Fellow, IEEE), DOMINIQUE SCHREURS[2], (Fellow, IEEE), AND HENDRIK ROGIER[1], (Senior Member, IEEE)

[1]IDLab, Electromagnetics Group, Department of Information Technology, Ghent University-imec, B-9052 Ghent, Belgium
[2]Division ESAT-TELEMIC, Katholieke Universiteit Leuven, B-3001 Leuven, Belgium

Corresponding author: Kamil Yavuz Kapusuz (kamilyavuz.kapusuz@ugent.be)

This work was supported by the European Research Council, through ATTO: A New Concept for Ultrahigh Capacity Wireless Networks, under Grant 695495.

ABSTRACT The Internet of Things requires highly efficient ultra-wideband antenna systems that yield high performance at low manufacturing cost. Therefore, a novel ultra-wideband circular air-filled substrate-integrated-waveguide (AFSIW) cavity-backed annular slot antenna is proposed that enables straightforward integration into general-purpose materials by means of standard manufacturing techniques. The cavity top plane, serving as antenna aperture, contains two concentric annular slots, both split into two by shorting tabs that create a virtual electric wall. This enables the generation of a $TE_{11,slot}$ even mode in both parts of each annular slot, giving rise to a conical radiation pattern. By exciting two such modes and judiciously positioning their resonance frequencies, all the unlicensed national information infrastructure (U-NII) [5.15–5.85] GHz radio bands are covered. The annular slot antenna is then made polarization reconfigurable through an innovative excitation of the slot modes by replacing the shorting tabs with four pairs of the PIN diodes. These dynamically switch between two orthogonal linear polarizations by changing the dc control current at the antenna RF port through an external bias tee. This simple, yet effective, bias network enables the integration of all polarization control electronics inside the antenna cavity to protect them from environmental effects. A low-cost antenna substrate was realized through standard additive manufacturing in a 3D-printed substrate, while a standard high-frequency laminate was used to implement the upper conducting plane containing the radiating elements and the polarization reconfiguration electronics. The antenna features an impedance bandwidth of 0.93 GHz, a front-to-back ratio of 14 dB, a total antenna efficiency higher than 95%, and 4.9 dBi gain for each polarization state.

INDEX TERMS Additive manufacturing, air-filled substrate-integrated-waveguide (AFSIW), cavity-backed slot antenna, circular cavity, in-cavity electronics, PIN diode, partially-filled circular waveguide, polarization reconfiguration, reconfigurable antenna, substrate-independent, ultra-wideband.

I. INTRODUCTION

The Internet of Things (IoT) entails the concept of a worldwide infrastructure of interconnected everyday devices or objects, augmented with additional functionality, such as sensing, processing and wireless communication [1]. An energy-efficient and stable wireless communication link is essential for each of these smart objects to implement reliable communication in realistic deployment scenarios [2].

The associate editor coordinating the review of this manuscript and approving it for publication was Kai Lu.

Moreover, these wireless communication systems should be compact and exhibit ultra-wideband performance to provide the data rates needed by the various types of future emerging wireless applications [3], while exhibiting a stable *conical beam pattern* with a null at zenith and peaking at an intermediate elevation angle, allowing reliable communication between a user and an interrogator integrated in smart surfaces (floors/ceilings/desks) [4]–[6]. The system's dimensions should facilitate invisible integration into these objects [7]. In addition, new fabrication technologies should be developed to pervasively co-integrate antennas,

microwave components and electronic circuits within everyday objects to realize unprecedented performance at low manufacturing cost by exploiting low-cost, general-purpose materials [8].

The integration of dynamic polarization reconfiguration functionality on a single feed antenna is vital to guarantee reliable wireless communication in a compact footprint. Therefore, a significant number of polarization reconfigurable antennas were developed in recent years [9]–[22]. It is generally accepted that switching between different feed line configurations is a poor solution, since system size and complexity rapidly increase with the number of switching states [9]–[11]. In addition, several electromagnetic interference (EMI) issues may arise due to unwanted leakage [12]–[15]. On the one hand, a variety of reconfigurable radiators has been proposed that reduce complexity, size and EMI issues. However, most of these solutions suffer from narrow impedance bandwidth and/or from degraded performance when integrated into everyday devices [16]–[21]. On the other hand, substrate integrated waveguide (SIW) technology demonstrates great potential to realize robust and high-performance antenna elements [23], microwave components [24], and even complete systems [25]. Various bandwidth enhancement techniques for SIW antennas have been developed to meet the demanding requirements of the current and next generation IoT applications [26], [27]. Moreover, to minimize cost, SIW components and antennas may be implemented on commercially-available, general-purpose materials, such as paper [28], textiles [29], and plastics [30]. However, the high losses and frequency-dependent properties of these materials significantly decrease the performance of conventional dielectric-filled SIW-based systems. Therefore, a substrate-independent air-filled SIW (AFSIW) architecture was proposed in [31] to enable direct and robust integration of high-performance microwave components into commercially available general-purpose materials.

In this paper, an innovative single-feed polarization-reconfigurable ultra-wideband substrate-independent AFSIW cavity-backed slot antenna with conical radiation pattern is proposed for high-performance smart surface applications. The conical radiation pattern is achieved by adding two diametrically opposed conducting shorting tabs to an annular slot topology. The modes in the resulting two half-rings generate magnetic currents with opposite polarity, in contrast to the conventional annular slot antenna where magnetic currents with the same polarity produce a broadside radiation pattern. By activating the appropriate metal shorting tabs through diodes, the desired antenna polarization is selected. The antenna covers the frequency band from 5.15 GHz to 5.85 GHz. To streamline the design flow, we first derive an analytical expression for the effective permittivity and loss tangent of circular AFSIWs and cavities based on modal analysis. This allows designers to control the effective permittivity and loss tangent by adequate selection of the air-filled region within the circular cavity. For this purpose, novel design guidelines are provided to minimize losses and to maximize radiation efficiency, while guaranteeing a compact, cost-effective and low-profile design. The potential of this approach is then exploited to realize a novel multi-mode AFSIW circular cavity with multiple radiating ring slots to achieve ultra-wideband performance. In particular, the single-feed ultra-wideband antenna enables dynamic reconfiguration between two orthogonal linear polarizations by means of four pairs of PIN diodes, judiciously positioned inside the air-filled antenna cavity, and controlled by a simple, yet effective, bias network. By simply changing the polarity of the DC control current at the antenna RF port through an external bias tee, the antenna switches between orthogonal linear polarizations. To the authors' best knowledge, this is the first antenna with conical radiation pattern that features substrate-independent, wideband antenna performance and dynamic polarization reconfigurability through electronic components exclusively deployed *inside* the cavity.

The novel antenna design paradigm features (i) substantial loss reduction owing to the AFSIW topology and simplified biasing network, (ii) a dedicated design procedure based on a novel analytical formula for the effective permittivity and loss tangent of circular AFSIW cavities, (iii) protection of the PIN diodes without radome by integrating the electronic components inside the cavity, (iv) stable ultra-wideband [defined by the U.S. Federal Communications Commission (FCC) in [32] as a signal with an instantaneous spectral occupancy in excess of 500 MHz or a fractional bandwidth of 20% or more] impedance matching for both polarization states without additional reconfigurable matching networks because of the symmetric antenna topology, and (v) low component count as there is no need for additional capacitors/inductors to isolate the DC bias from the RF signals, owing to the dedicated antenna topology. In contrast to [31], where design rules are described and waveguides, a splitter and a coaxial-to-air-filled SIW transition are developed in rectangular cavities, in this paper, the substrate-independent AFSIW technology is applied to an antenna implemented in a circular cavity, based on novel, dedicated design formulas.

The remainder of the paper is organized as follows. Section II describes the design of the single linearly-polarized AFSIW cavity-backed slot antenna, and discusses all relevant design parameters, including propagation constant and loss factors. Section III elaborates on the design flow to extend the functionality of the single linearly-polarized design towards a polarization-reconfigurable design with the electronic components integrated inside the cavity. Section IV discusses the measurement results. Finally, conclusions are drawn in Section V.

II. LINEARLY-POLARIZED AIR-FILLED SIW CAVITY-BACKED SLOT ANTENNA

A. ARCHITECTURE

The proposed antenna geometry is shown in Fig. 1. An additive-manufacturing-enabled SIW cavity-backed slot

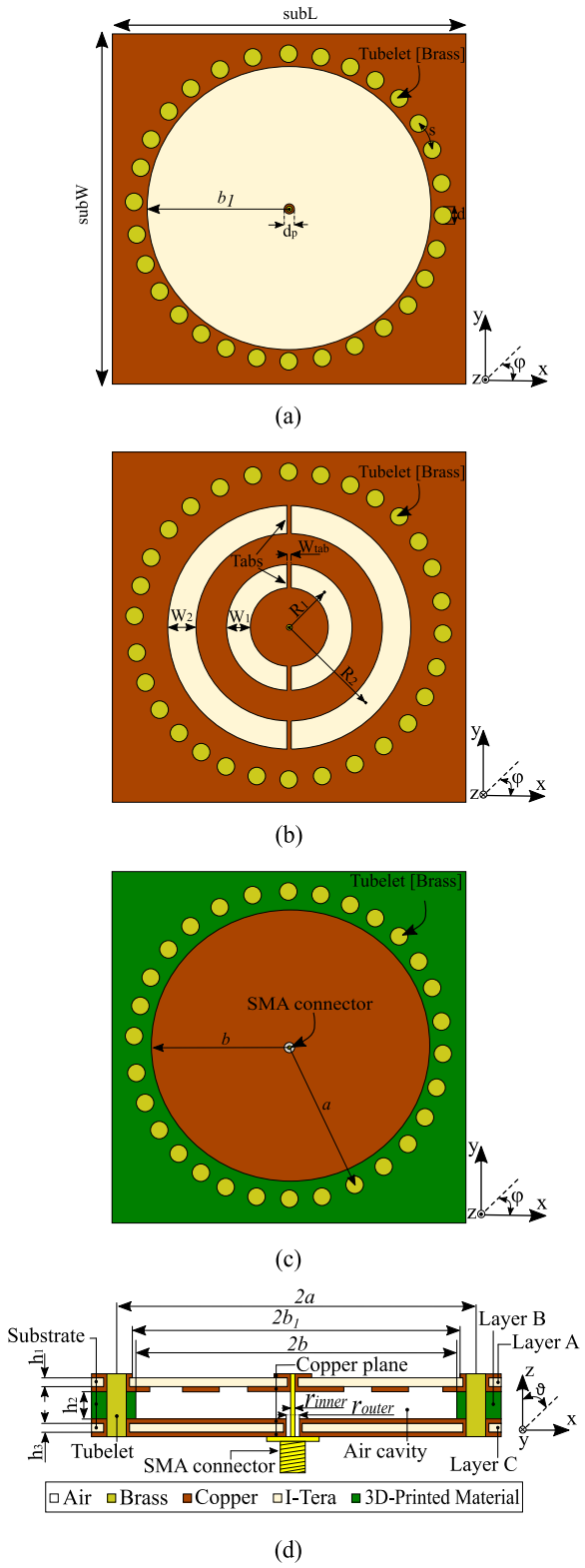

FIGURE 1. AFSIW cavity-backed slot antenna element. (a) Front side of Layer A. (b) Back side of Layer A. (c) Horizontal cross-section. (d) Vertical cross-section.

antenna topology is adopted to minimize backward radiation, to maximally suppress surface waves, and to guarantee excellent isolation from its surroundings, while exploiting the advantages of planar technology, being a low profile, low fabrication cost, rapid manufacturing, and easy integration with other planar circuitry. However, in contrast to conventional high-frequency PCB laminates, the materials applied in low-cost additive manufacturing processes (PLA, TPE, ABS, Nylon, ...) do not always exhibit favorable characteristics to be used as substrates for dielectric-filled SIW antennas, due to their inhomogeneous character and higher dielectric loss [33]. Moreover, the permittivity and loss tangent of these materials vary with the material's extrusion speed, temperature [34] and infill percentage [33], [35]. Therefore, we adopt the substrate-independent SIW technology proposed in [31] for rectangular cavities to implement the novel circular AFSIW cavity-backed antenna.

The resulting antenna topology maintains the advantages of conventional dielectric-filled SIW antennas while providing high efficiency, independent from the material in which the antenna substrate is manufactured. In particular, to realize an AFSIW cavity-backed antenna, three dielectric layers (Layer A, Layer B, Layer C) and four conductor layers are required, as shown in Fig. 1. The main purpose of the upper (Layer A) and lower (Layer C) dielectric layers is to provide support to the top and bottom conducting boundaries of the cavity. They sandwich the middle dielectric layer (Layer B), realizing an air-filled region, by means of an array of metallic vias, implemented by tubular eyelets (or tubelets), which also tighten the complete layer stack. The air-filled region is judiciously designed in Layer B to minimize the dielectric loss of the low-cost 3D-printed material, as to obtain a highly efficient antenna. A small dielectric supporting region inside the waveguide must be preserved to guarantee sufficient mechanical strength. By ensuring that the strongest electromagnetic fields occur in the air-filled region, the antenna performance becomes nearly substrate independent, as demonstrated in Section II.D. A standard SMA connector is used to feed the antenna. Its inner conductor is soldered to the upper conductor of Layer A, whereas connection between the top and bottom conductor surface of Layer A is ensured by plated holes [Fig. 1(d)]. The outer conductor of the coaxial probe is soldered to the conducting ground plane of the cavity, supported by Layer C. As can be seen from Fig 1(d), Layer C is not a part of the antenna cavity, which allows us to exploit a low-cost dielectric material to realize this layer. RF components may also be integrated below the antenna ground plane of this layer in future active designs. Second, the antenna topology provides excellent ultra-wideband characteristics, achieved by tuning the air-filled substrate's thickness h_2. Inherently, the length of the tubelets and the thickness of Layer B, h_2, determine the height of the SIW sidewalls. Consequently, AFSIW cavities with arbitrary height can be easily constructed by 3D-printing material with the desired thickness and selecting appropriate tubelets. As the impedance bandwidth is directly proportional to the cavity height for air-filled cavity-backed slot antennas, the antenna's impedance bandwidth can be enlarged by increasing the substrate thickness h_2 of Layer B, as specified in [26].

B. ANTENNA TOPOLOGY AND OPERATION PRINCIPLE

A circular cavity topology is selected to exploit the azimuthal symmetry of the cavity modes. To realize a highly-efficient antenna with a conical beam radiation pattern covering an ultra-wide −10 dB impedance bandwidth, the antenna topology shown in Fig. 2 is adopted. As a starting point, a circular cavity is coaxially fed at its center [36], such that only radially symmetric $TM_{0m,\text{waveguide}}$ modes are excited by the transverse electromagnetic (*TEM*) mode that is incident via the coaxial cable [Fig. 2(a)]. The cavity radius is dimensioned such that only its fundamental mode, $TM_{01,\text{waveguide}}$, whose transverse electric field is shown in Fig. 3(a), is propagating in the circular cross-section of the cavity. The pertinent design procedure is outlined in Section II-E. It is based on the formulas derived for circular AFSIWs in Section II-C and Section II-D.

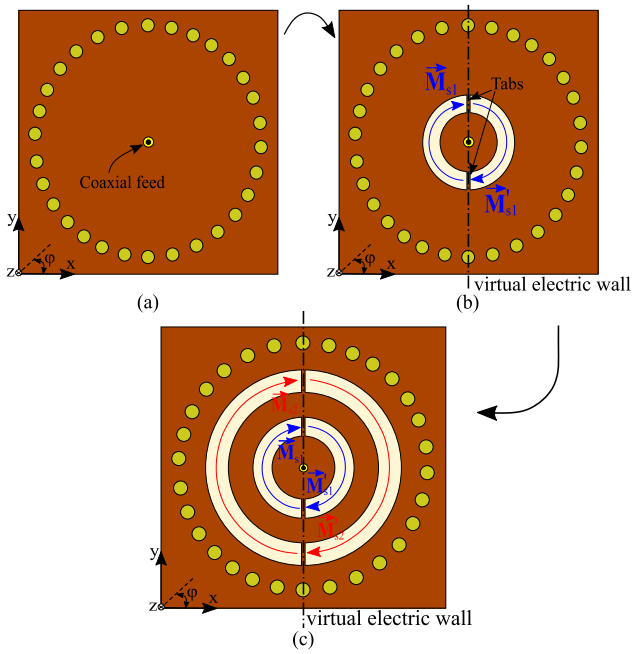

FIGURE 2. Design evolution of a single-feed AFSIW cavity-backed slot antenna with ultra-wide bandwidth and conical-beam radiation pattern. (a) Step 1: Circular cavity fed by a coaxial probe at its center. (b) Step 2: Linearly-polarized radiation is obtained by inserting a resonant annular ring slot in the top plane of the cavity and exploiting two diametrically positioned shorting tabs.(c) Step 3: Additional radiating ring with shorting tabs is positioned to improve impedance bandwidth of the antenna.

Next, a resonant annular slot is designed in the top plane of the cavity, as shown in Fig. 2(b). The $TE_{11,\text{slot}}$ odd mode in a conventional annular ring slot antenna [Fig. 3(d)] excited by a microstrip line [Fig. 3(c)], as in [37], is less appropriate for smart surface applications, since it mainly radiates along the broadside direction. Moreover, the antenna topology in [37] radiates electromagnetic fields in both hemispheres ($z>0$ and $z<0$), which makes it difficult to avoid parasitic coupling when integrating active components in proximity of the antenna. In our application, the $TE_{11,\text{slot}}$ even mode is required [4] because this generates a radiation pattern with a null in the broadside direction, providing better coverage. Hence, two diametrically positioned shorting tabs are added to split the annular slot in two. In each half-ring radiating aperture, the $TM_{01,\text{waveguide}}$ mode propagating in the circular cross-section of the feeding cavity [Fig. 3(a)] is converted into the $TE_{11,\text{slot}}$ even mode [Fig. 3(b)] of that slot. As seen in the transverse electric field profile of Fig. 3(b), the *yz*-plane formed by both perfect electrically conducting (PEC) shorting tabs acts as an electric wall, mirroring the modal field profile from one half-ring slot into the other, such that the combination of both half-ring radiating slots acts as a half-wavelength magnetic quadrupole. Consequently, in contrast to the broadside radiation pattern generated by the conventional annular ring slot antenna [Fig. 3(d)], now a conical beam radiation pattern is produced by the magnetic currents $\vec{M}_s$. The angular location of the shorting tabs defines the direction along which the electric field is linearly polarized, given the symmetry of the structure (for example, the antenna topology shown in Fig. 2(b) exhibits *x*-oriented linear polarization).

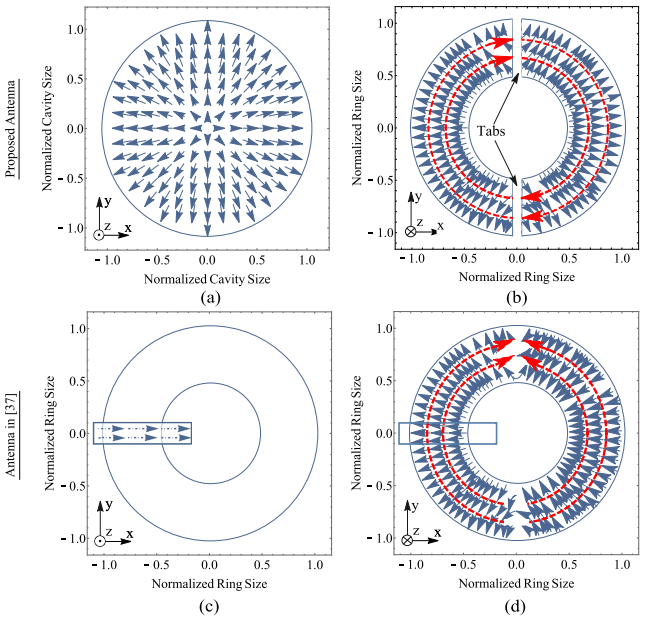

FIGURE 3. Transverse electric field (solid blue arrows) and magnetic currents (dashed red lines) of the mode profiles present in the novel antenna topology: (a) $TM_{01,\text{waveguide}}$ mode propagating in the circular cross-section of the cavity feeding the radiating slots, (b) $TE_{11,\text{slot}}$ mode in both annular half ring slots generated by the two PEC shorting tabs. Transverse electric field (solid blue arrows) and magnetic currents (dashed red lines) of the mode profiles present in the conventional annular slot antenna in [37]: (c) the flow of electric current (dash dotted line) in the microstrip line serving as a feed section, (d) $TE_{11,\text{slot}}$ odd mode in the annular slot.

Since cavity-backed slot antennas mainly exhibit narrowband behavior [38], two annular slots, as shown in Fig. 2(c), are required in the antenna's top plane to cover the entire Unlicensed National Information Infrastructure (U-NII) radio communication band [37]. The double-ring of slots produces two distinct resonances whose frequencies are carefully positioned in the [5.15-5.85]-GHz band, as to achieve ultra-wideband performance. Due to the loading effect of the antenna cavity and the interaction between both slots, their

resonance frequencies will differ significantly from those of a stand-alone ring antenna, which satisfy [39]

$$J_n'(kr_o)Y_n'(kr_i) - Y_n'(kr_o)J_n'(kr_i) = 0 \tag{1}$$

where r_i and r_o denote the inner and outer radius of the annular ring-slot, k is the wave number, and J_n and Y_n represent the n^{th}-order Bessel function of the first kind and second kind, respectively.

Since the loading effect by the cavity plays an important role, the interplay between cavity and slot modal fields makes the relationship between resonance frequencies and annular slot dimensions much more complicated than expressed by (1). Therefore, each resonance frequency was carefully controlled by adapting the physical parameters of the annular slots with shorting tabs. The inner annular slot with shorting tabs is dimensioned such that it produces a resonance at 5.15 GHz. Next, the size of the outer slot is selected such that a second resonance occurs at 5.85 GHz. Fig. 4(a) and Fig. 4(c) show that the electric field at the lowest resonance frequency is mainly concentrated in the inner slot, while being weak in the outer slot and in the cavity. In this case, the cavity sidewalls only have a small effect on the resonant field. In contrast, at 5.85 GHz, the electric field is strong in both slots and in the cavity. As shown in Fig. 4(b) and Fig. 4(d), at 5.85 GHz, the cavity field distribution generates significant tangential electric field contributions in both the small and the large annular half ring slots, contributing to the antenna radiation. Both resonances yield a large E-field across one or both slots, producing the desired radiation pattern and required polarization. For the optimized dimensions in Fig. 4 and the annotated parameters in Fig. 1, a broad impedance bandwidth, covering the [5.15 - 5.85] GHz band, is achieved.

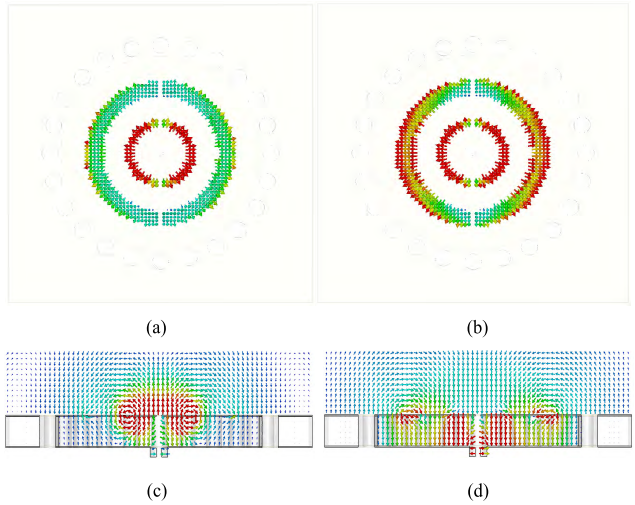

FIGURE 4. Simulated hybrid mode profiles: electric field [V/m]. Horizontal cross sections of the proposed antenna at (a) 5.15 GHz and (b) 5.85 GHz. Vertical cross sections of the proposed antenna at (c) 5.15 GHz and (d) 5.85 GHz. Optimized dimensions: $sub_W = sub_L = 75.0$ mm, $a = 27.25$ mm, $b = b_1 = 24.53$ mm, $R_1 = 7.55$ mm, $W_1 = 1.7$ mm, $R_2 = 16.3$ mm, $W_2 = 4.0$ mm, $W_{tab} = 0.2$ mm, $h_1 = h_3 = 0.25$ mm, $h_2 = 6.5$ mm, $d = 4.0$ mm, $d_p = 2.3$ mm, $s = 5.7$ mm, $r_{inner} = 1.3$ mm, $r_{outer} = 4.3$ mm. Substrate parameters at 5.5 GHz: Layers A and C are implemented in I-Tera ($\epsilon_r = 3.43$, $\tan\delta = 0.014$), Layer B is implemented in 3D-printed material with infill percentage of 50% ($\epsilon_r = 2.0$, $\tan\delta = 0.03$).

To provide insight about the effect of the shorting tabs on the radiation pattern and the polarization of the electric field, Fig. 5 compares the AFSIW cavity-backed slot antenna without shorting tabs [Fig. 5(a)] to its counterpart with shorting tabs added along the y-direction [Fig. 5(b)] and the x-direction [Fig. 5(c)]. Without shorting tabs, the radiation pattern is rotationally symmetric along the z-axis and the electric field is polarized along the θ direction [Fig. 5(d)]. The shorting tabs break the symmetry, leading to a pattern that is no longer omnidirectional in the azimuth plane. Fig. 5(e) shows that the electric field is predominantly polarized along the x-direction for y-oriented tabs, while being mainly y-polarized [Fig. 5(f)] for tabs in the x-direction.

C. MODAL ANALYSIS OF CIRCULAR AFSIW

The performance of the proposed antenna topology strongly depends on the portion of Layer B's dielectric material remaining inside the cavity to provide mechanical robustness. This area, with surface $\pi a^2 - \pi b^2$, is colored in green in Fig. 1(c). In Layer B, the electromagnetic field of the lower-order modes [Fig. 3(a)] is mainly confined in the central air region, while being weak near the edge. Therefore, the effect of the small lossy dielectric region inside the cavity can be neglected as long as the ratio of the constructed air-cavity diameter, $2b$, over the actual cavity diameter, $2a$, [Fig. 1(d)] remains above a certain threshold, such that $b/a \lessapprox 1$.

Let us, therefore, focus on the transmission of electromagnetic waves in the guided section, being a circular waveguide implemented in AFSIW manufacturing technology. Fig. 6(b) shows the cross-section under study, while Fig. 6(a) depicts the cross-section of an equivalent circular waveguide partially filled with lossy dielectric (specifically 3D-printed material in this paper) with thickness t, permittivity ϵ_c and permeability μ_c. The inner air region (relative permittivity ϵ_0 and permeability μ_0) extends up to radius b. The equivalent waveguide's boundary consists of a PEC wall at radius a_{eff}.

The structure in Fig. 6(a) generally supports hybrid (HE) modes, besides transverse electric (TE) and transverse magnetic (TM) modes. However, the rows of vertical tubelets in Fig. 6(b) do not support modes that generate φ-oriented currents in the sidewalls. Therefore, only TM_{nm} modes with $n = 0$ should be used in these types of waveguides. For these modes propagating along the z-direction with propagation factor $e^{-\gamma z}$, the propagation constants γ satisfy [40]

$$\gamma^2 = \epsilon_0\mu_0 k_0^2 - k_{\rho,1}^2 = \epsilon_c\mu_c k_0^2 - k_{\rho,2}^2 \tag{2}$$

where $k_{\rho,1}$ and $k_{\rho,2}$ are the radial part of the wave vectors in air and dielectric, respectively. $k_0 = 2\pi/\lambda_0$ is the free-space wave number and λ_0 is the free-space wavelength. The dispersion relation of these TM_{0m} modes simplifies to

$$\frac{\epsilon_c}{k_{\rho,2}}\frac{a_{TM}}{b_{TM}} - \frac{\epsilon_0}{k_{\rho,1}}\frac{J_0'(k_{\rho,1}b)}{J_0(k_{\rho,1}b)} = 0 \tag{3}$$

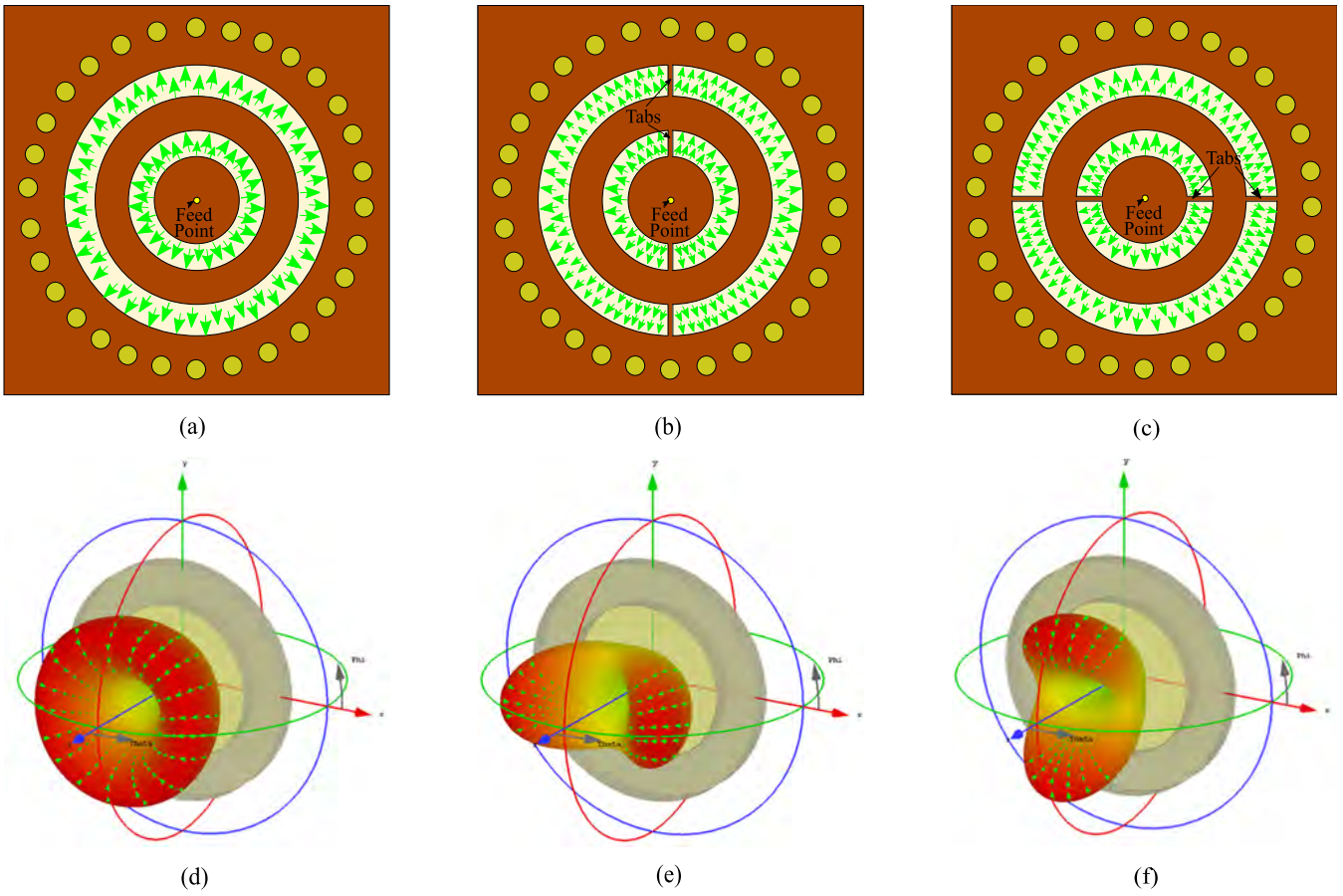

FIGURE 5. AFSIW cavity-backed slot antenna: (a) *without* symmetrically positioned shorting tabs, (b) *with* shorting tabs oriented in *yz*- plane (*x*-oriented polarization state), (c) *with* shorting tabs oriented in *xz*- plane (*y*-oriented polarization state). 3D gain pattern of the antenna on a linear scale. In all gain patterns, the $|E_\theta|$ is the main component of the electric field ($|E_\varphi| \ll |E_\theta|$). (d) A circular AFSIW cavity-backed annular slot antenna *without* shorting tabs. Proposed circular AFSIW cavity-backed annular slot antenna *with* shorting tabs: (e) *x*-oriented polarization state, (f) *y*-oriented polarization state.

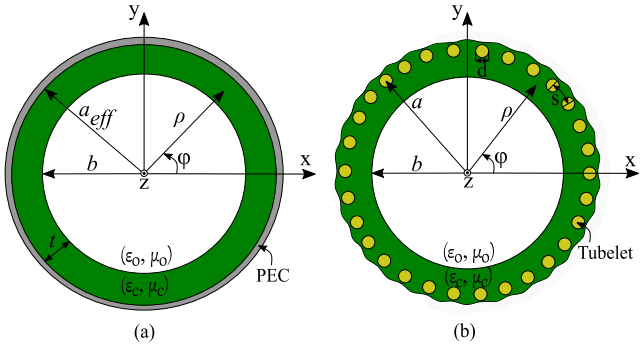

FIGURE 6. (a) Cross-sectional view of a circular waveguide partially filled with a dielectric material, (b) Cross-sectional view of a circular AFSIW.

with

$$\begin{cases} a_{TM} = J_0(k_{\rho,2}a_{eff})H_0^{(2)'}(k_{\rho,2}b) - H_0^{(2)}(k_{\rho,2}a_{eff})J_0'(k_{\rho,2}b) \\ b_{TM} = J_0(k_{\rho,2}a_{eff})H_0^{(2)}(k_{\rho,2}b) - H_0^{(2)}(k_{\rho,2}a_{eff})J_0(k_{\rho,2}b) \end{cases}$$

where J_0 denotes the 0^{th}-order Bessel function of the first kind and $H_0^{(2)}$ represents the 0^{th}-order Hankel function of the second kind.

For small relative effective thicknesses t/b of the supporting sidewalls, the proposed AFSIW behaves as a homogeneous waveguide with an effective complex permittivity $\epsilon_{c,\text{eff}}$, which takes value between 1 and ϵ_c. Subsequently, a perturbation analysis is applied to accurately obtain the effective permittivity of the circular AFSIW with a thin layer of lossy dielectric ($t \ll b$),

$$\epsilon_{c,\text{eff}} \approx 1 + \xi_1\, t + \xi_2\, t^2 + \xi_3\, t^3 + \xi_4\, t^4, \quad \text{for } t \ll b \quad (4)$$

with

$$\begin{cases} \xi_1 = \dfrac{2(\epsilon_c - 1)(k_0^2 a^2 - \chi_{0m}^2)}{\epsilon_c k_0^2 a^3} \\ \xi_2 = \dfrac{(\epsilon_c - 1)(2(\epsilon_c - 1)k_0^4 a^4 + \epsilon_c k_0^2 a^2 \chi_{0m}^2 + (2 - 3\epsilon_c)\chi_{0m}^4)}{\epsilon_c^2 k_0^2 a^4 \chi_{0m}^2} \\ \xi_3 = \dfrac{A(\epsilon_c - 1)}{3\epsilon_c^3 k_0^2 a^5 \chi_{0m}^4} \\ \xi_4 = \dfrac{B(\epsilon_c - 1)}{6\epsilon_c^4 k_0^2 a^6 \chi_{0m}^6} \end{cases}$$

where χ_{0m} represents the m^{th} zero ($m = 1, 2, 3, \ldots$) of Bessel function J_0 of the first kind and of order zero.

$$A = 2[8(\epsilon_c-1)^2k_0^6a^6-(\epsilon_c-1)k_0^4a^4(3(\epsilon_c-2)+(\epsilon_c-1)k_0^2a^2)\chi_{0m}^2+k_0^2a^2(\epsilon_c^2+(\epsilon_c-1)(\epsilon_c^2-3)k_0^2a^2)\chi_{0m}^4 + \ldots(7\epsilon_c-6\epsilon_c^2-2+(2\epsilon_c^2-3)k_0^2a^2)\chi_{0m}^6+(\epsilon_c+1)\chi_{0m}^8]. \quad (4a)$$

$$B = [108(\epsilon_c-1)^3k_0^8a^8-2(\epsilon_c-1)^2k_0^6a^6(8(5\epsilon_c-8)+9(\epsilon_c-1)k_0^2a^2)\chi_{0m}^2 + \ldots(\epsilon_c-1)k_0^4a^4(24-12\epsilon_c-\epsilon_c^2+2(20+\epsilon_c(-25+\epsilon_c+4\epsilon_c^2))k_0^2a^2)\chi_{0m}^4+3k_0^2a^2(\epsilon_c^3+2(\epsilon_c^2-3\epsilon_c+2)k_0^2a^2)\chi_{0m}^6 + \ldots(4-24\epsilon_c+47\epsilon_c^2-30\epsilon_c^3+2(12+\epsilon_c(-9+4\epsilon_c(-3+2\epsilon_c)))k_0^2a^2)\chi_{0m}^8+2(-7+8\epsilon_c^2)\chi_{0m}^{10}]. \quad (4b)$$

The coefficients A and B are defined by (4a) and (4b), as shown at the top of this page. The effective thickness t of the lossy material serving as sidewall support in AFSIW may be approximated by [41]

$$t = a - b - \frac{d^2}{0.95s} \quad (5)$$

where d is the diameter of the tubelets forming the sidewalls and s represents the spacing between two tubelets.

Notice that, in contrast to propagation in rectangular AFSIWs [31], the dielectric constant of the lossy 3D-printed material inside the waveguide starts to affect the effective permittivity from the linear term in t. Therefore, low-loss circular AFSIW designs require thinner dielectric regions inside the waveguide than their rectangular equivalents.

By inserting $\epsilon_{c,\text{eff}}$ into (2) and rearranging the terms, we obtain following approximation for the propagation constant in case of a small relative effective thickness t/b of the supporting sidewalls

$$\gamma^2 \approx \epsilon_{c,\text{eff}}k_0^2 - \left(\frac{\chi_{0m}}{b+t}\right)^2 \quad (6)$$

A relation between the resonance frequencies of the TM_{0m} modes and the cavity dimensions can be derived directly by means of a transverse resonance technique

$$f_{c,0m} \approx \frac{c}{2\pi\sqrt{\epsilon_{c,\text{eff}}}}\sqrt{\left(\frac{\chi_{0m}}{a}\right)^2} \quad (7)$$

where c is the speed of light in free space.

D. DESIGN OF ANTENNA CAVITY

Based on the modal analysis in Section II.C, we propose a design procedure to determine the threshold value of b/a above which the antenna cavity can be assumed to be substrate independent, given the substrate's material parameters. Therefore, we first apply the matrix-pencil two-line method in [42] to characterize the dielectric properties of the adopted 3D-printed material, as permittivity and loss tangent are typically not readily available in a datasheet. In this paper, one of the most common and cost-effective materials for 3-D printing, polylactic acid (PLA), is selected as a dielectric substrate (Layer B). In the [5.15 - 5.85] GHz frequency band, the characterization procedure yields an estimated (ϵ_r, tanδ) of (1.65, 0.015), (2.0, 0.03) and (3.05, 0.05) for an infill percentage of 25%, 50%, and 100%, respectively.

Inserting the nominal dielectric permittivity and loss tangent values into (4) yields the approximate effective dielectric constant and loss tangent of a circular AFSIW with PLA-supporting sidewalls, whereas (3) yields the exact values. Fig. 7 shows the exact loss tangent as a function of the effective thickness (t/λ_0) of the 3D-printed material with infill percentage of 50% sidewalls for a waveguide with radius $a = 0.58\lambda_0$ [radius a is obtained by applying (7) at the center frequency of the monomodal operational bandwidth of TM_{01} mode in a circular AFSIW], along with the third and fourth-order approximations. Good agreement between the exact result and the fourth-order approximation is observed. Hence, the fourth-order approximation is ideally suited to calculate the relative thickness ratio t/λ_0 that guarantees acceptably low dielectric losses and substrate independent behavior. In this paper, we ensure that the effective loss tangent remains below 10^{-3} [level typically encountered in high-frequency laminates] by fixing the relative thickness ratio to $t/\lambda_0 = 0.03$, corresponding to $t/b = 0.05$. Moreover, leakage loss can be kept reasonably small by exploiting brass tubelets that are spaced closely enough. For the latter, we apply the design rule based on the condition that the center-to-center spacing between neighboring tubelets s and the tubelet diameter d is sufficiently small (the condition $s/d < 2$ is given in [24]).

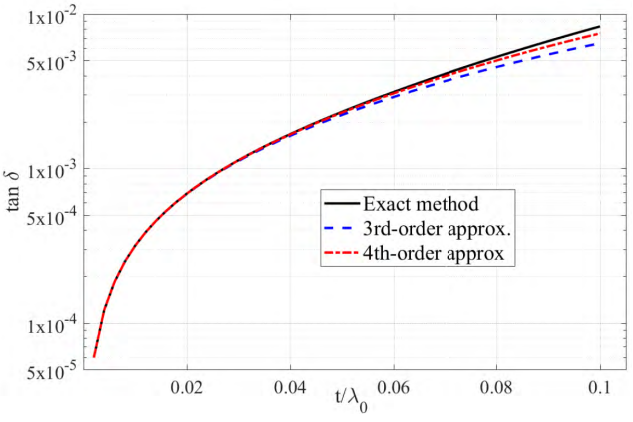

FIGURE 7. Effective loss tangent of the TM_{01} mode in a circular AFSIW with a radius $a = 0.58\lambda_0$ as a function of the effective thickness t/λ_0 of the supporting side walls. Layer B is implemented in PLA material by means of 3-D printing (Infill percentage of 50%).

In this paper, we select a waveguide radius of $a = 0.58\lambda_0$ and low-cost brass tubelets with a diameter $d = 4$ mm.

TABLE 1. Effective dielectric contrast and effective loss tangent of a circular AFSIW implemented in polylactic acid (PLA) for different infill percentages and relative effective thicknesses t/b of the supporting side walls.

t/b	$\Delta\epsilon_{r,\text{eff}}$			$\tan\delta_{\text{eff}}$		
	PLA (25% Infill)	PLA (50% Infill)	PLA (100% Infill)	PLA (25% Infill)	PLA (50% Infill)	PLA (100% Infill)
0.010	4.13e-3	5.3e-3	7.1e-3	9.6e-5	1.60e-4	1.77e-4
0.025	0.010	0.013	0.018	2.5e-4	4.18e-4	4.78e-4
0.050	0.021	0.028	0.039	5.3e-4	9.09e-4	0.001
0.075	0.033	0.043	0.061	8.4e-4	0.0015	0.002
0.100	0.044	0.059	0.088	0.0012	0.0022	0.003
0.125	0.056	0.076	0.117	0.0016	0.0030	0.005

The relative spacing between tubelets is set to $s/d = 1.42$. Substituting all values into (4) and (5) to account for the effect of the tubelets, yields an estimated radius ratio of $b/a \approx 0.9$. Table 1 confirms that, for these values, substrate independent performance is obtained as well as an effective loss tangent below 10^{-3}. Finally, the conductor and surface roughness losses may be reduced to the bare minimum by polishing the surface of the copper cladding of Layer A and Layer C with a highly conductive material (i.e. silver) before assembly.

E. DESIGN PROCEDURE

To achieve the desired ultra-wideband, substrate-independent, antenna performance, we adopt the design procedure proposed in Fig. 8. The design procedure, including material characterization, consists of six straightforward steps. First, we apply a matrix-pencil two-line method [42] to characterize the dielectric properties of the substrate materials under consideration. Second, these material characteristics are used to calculate the effective dielectric constant and the effective loss tangent of a circular AFSIW based on (4). Third, making use of the guidelines outlined in Section II.D, the relative via spacing, s/d, is fixed such that its value remains smaller than 2, thereby keeping the leakage loss sufficiently small. Then, the cavity radius, a, is calculated in the fourth design step by applying (7), ensuring monomodal wave propagation of the TM_{01} mode into a circular AFSIW section forming the backing cavity of the antenna. In the next step, the dimensions of both annular ring slots are carefully determined. Evidently, the double-ring of slots produces two distinct resonances. Therefore, a computer-aided optimization is performed by means of CST Microwave studio for the slots' parameters, to obtain the required impedance bandwidth. This optimization procedure is based on an extensive set of parameter sweeps that analyze the influence of the slot dimensions on the antenna performance.

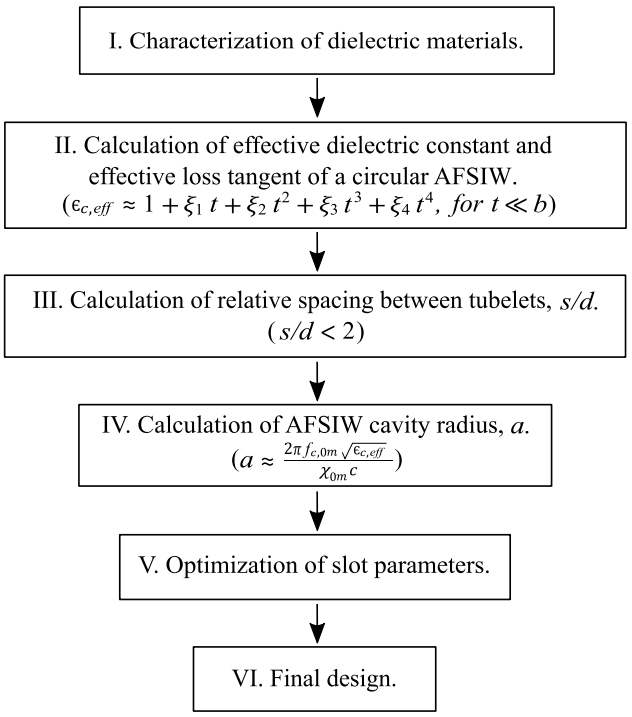

FIGURE 8. Design procedure of the proposed AFSIW-based antenna architecture.

Fig. 9 shows the results of the parametric analysis performed for the slot parameters R_1, W_1, R_2, and W_2, aiming to ensure that the proposed antenna covers the complete [5.15 - 5.85] GHz radio band. In detail, if the radius of the inner slot (R_1) decreases or the width of the inner slot (W_1) increases, there is more inductive coupling between inner slot and inner conductor of the SMA feed connector. Consequently, the lower resonance frequency increases, since the inner annular ring parameters mainly determine the smallest of both resonance frequencies. On the other hand, the amount of coupling between the two slots depends on the distance between them. An increase in the radius of the outer slot (R_2) reduces the coupling between the inner and outer slots. Therefore, the upper resonance frequency tends to increase when the inner and outer slots are further separated. Finally, it can be seen that an increase of the outer slot width (W_2) leads to an upward shift of the upper resonance frequency.

An additional parameter study is performed to assess the effects of cavity thickness on the antenna bandwidth performance. Fig. 10 depicts the relation between the fractional cavity height, $H_{cavity,frac} = h_2/\lambda_0$ where λ_0 is the free-space wavelength of the center frequency, and the fractional impedance bandwidth, for both the conventional dielectric-filled coaxial-probe-fed rectangular SIW cavity-backed slot antenna described in [43] and the proposed circular cavity-backed slot antenna. It can be seen that the impedance

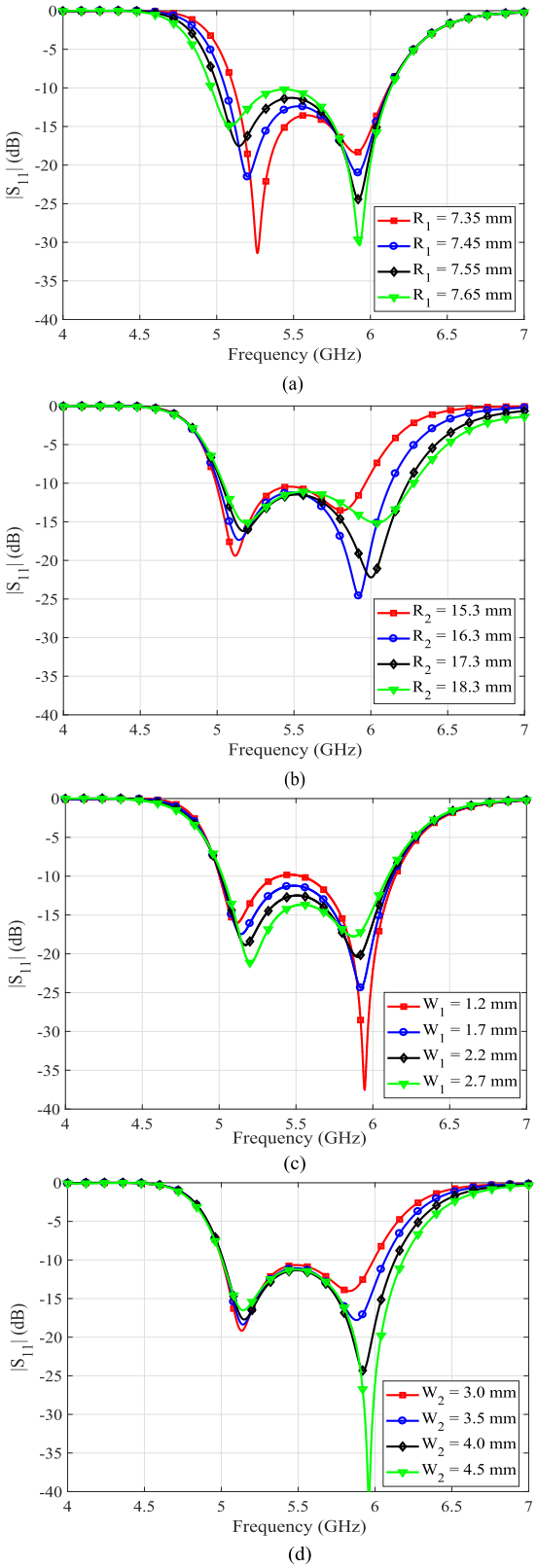

FIGURE 9. Influence of the slot dimensions on the magnitude of the reflection coefficient. (a) Inner annular slot radius, R_1. (b) Inner annular slot width, W_1. (c) Outer annular slot radius, R_2. (d) Outer annular slot width, W_2.

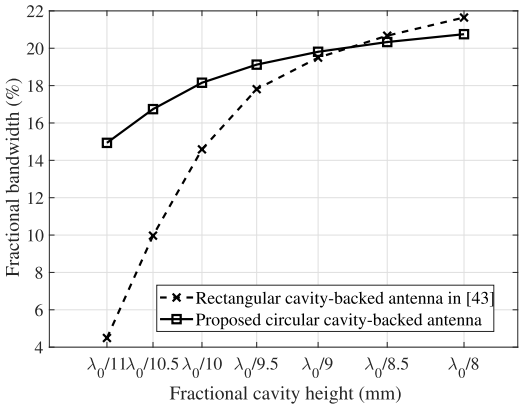

FIGURE 10. Comparison between the rectangular cavity-backed slot antenna in [43] and the proposed circular cavity-backed slot antenna based on simulation. Both designs exploit a coaxial feed and rely on a 3D-printed material with infill percentage of 50% ($\epsilon_r = 2.0$, tan$\delta = 0.03$) as antenna substrate.

bandwidth gradually enlarges for increasing cavity height. Moreover, the circular cavity yields a larger bandwidth up to a cavity height of $\lambda_0/9$ (∼6.5 mm). Above this value, the rectangular cavity-backed antenna has a slightly larger fractional bandwidth. As a result, our topology allows achieving the required bandwidth at a lower fractional cavity height. In addition, it provides better azimuthal symmetry, which permits the generation of circular polarization with better quality, particularly at low elevation angles, and it facilitates the design of polarization reconfigurable antenna topologies.

In a final step, we have analyzed the effect on the radiation pattern and polarization for the parameter variations considered in Fig. 9 and Fig. 10. The full-wave simulations have shown that the considered variations in slot dimensions and cavity thickness only have a marginal effect on the antenna radiation patterns.

III. POLARIZATION RECONFIGURABLE ANTENNA

A. REALIZATION OF RECONFIGURABLE POLARIZATION

The air-filled ultra-wideband SIW cavity-backed slot antenna topology proposed in previous section is now adapted as shown in Fig. 11, to implement compact and cost-effective reconfiguration between two orthogonal linear polarizations. Instead of fixing the polarization by the angular locations of small shorting tabs (with a width of W_{tab}) in Layer A [Fig. 1(b)], dynamic reconfiguration is achieved by replacing these short-circuits by PIN diodes at carefully selected angular positions [Fig. 11(b)].

Specifically, four pairs of PIN diodes are needed to switch between both (linear along x- or y-direction) polarization states. In this design, MACOM's MA4AGBLP912 PIN diodes are adopted as a switching element, because of their low resistance in forward-biased state and low capacitance in reverse-biased state. A bulky and intricate bias network is avoided by applying the bias to the antenna feed line through an external bias tee, as shown in Fig. 11(c).

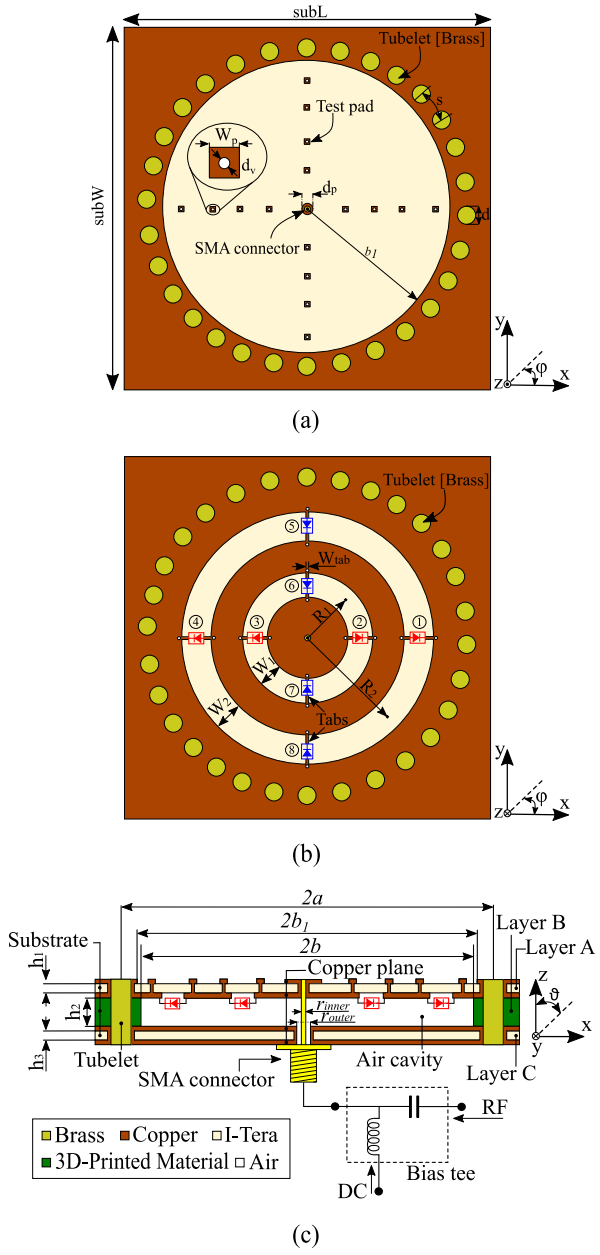

FIGURE 11. **Polarization reconfigurable AFSIW cavity-backed slot antenna element. (a) Front side of Layer A. (b) Back side of Layer A. (c) Cross-sectional view. Optimized dimensions: $sub_W = sub_L = 75.0$ mm, $a = 26.7$ mm, $b = 24.0$ mm, $R_1 = 6.3$ mm, $W_1 = 3.34$ mm, $R_2 = 17.0$ mm, $W_2 = 4.79$ mm, $W_{tab} = 0.2$ mm, $W_p = 1.2$ mm, $d_p = 2.1$ mm, $d_v = 0.6$ mm, $d = 4.0$ mm, $s = 6.45$ mm, $r_{inner} = 1.3$ mm, $r_{outer} = 4.3$ mm, $h_1 = h_3 = 0.25$ mm, $h_2 = 5.3$ mm.**

This implementation reduces the complexity and the parasitic effects of the biasing network and their control lines. In addition, no additional lumped (lossy) capacitors and/or inductors are needed to isolate the DC bias, while maintaining continuity for the RF signals. This task is already performed by the radiating slots in combination with a proper orientation of the PIN diodes. In this way, the proposed antenna is capable of switching its linear polarization from *x*- to *y*-oriented, or vice versa, by controlling the DC control current at the antenna RF port through the bias tee. When applying a positive DC current, the red-colored diodes (1, 2, 3, and 4) are brought in the ON state and the dark blue-colored diodes (5, 6, 7, and 8) are switched OFF [Fig. 11(b)], yielding an *y*-oriented linear polarization. Similarly, by reversing the polarity of the DC bias current, the red-colored diodes are switched OFF and the dark blue-colored diodes are brought in the ON state. Now, the antenna exhibits a *x*-oriented linear polarization. As a consequence, in each biasing state, only two pairs of diodes are forward polarized. All diodes are soldered using a standard soldering process. Under a magnifier lens, the components are positioned on the slits patterned at the center of the tabs to the bottom conductive layer of Layer A [Fig. 11(b)] before assembly of all layers. In the design, all patterned slits' length are selected equal to the diode length. Hence, all electronic components are robustly and invisibly integrated inside the antenna cavity, while being protected against environmental effects. Finally, small through-hole vias and copper test pads are introduced in the design to verify the PIN diode operation after assembly [Fig. 11(a)]. To the authors' best knowledge, this is the first time in literature that PIN diodes are placed inside the SIW antenna cavity.

During the computer-aided design process, the frequency domain solver of CST Microwave Studio is used as a full-wave simulator. Since the loading characteristics of the antenna cavity changes for different states of the diodes, the antenna impedance and the antenna radiation characteristics are optimized to the diode impedances for different states during the full-wave/circuit co-simulation. Therefore, we have initially performed TRL-calibrated diode measurements to determine the equivalent circuit model of the PIN diodes for each state. A symmetrical Π-equivalent model [Fig. 12(a)] was extracted to accurately model the PIN diodes [44]. The shunt branches of the model, Z_{p1} and Z_{p2}, are associated to the shunt fringing fields in the microstrip lines and not to the PIN diode itself. Hence, they are omitted in the

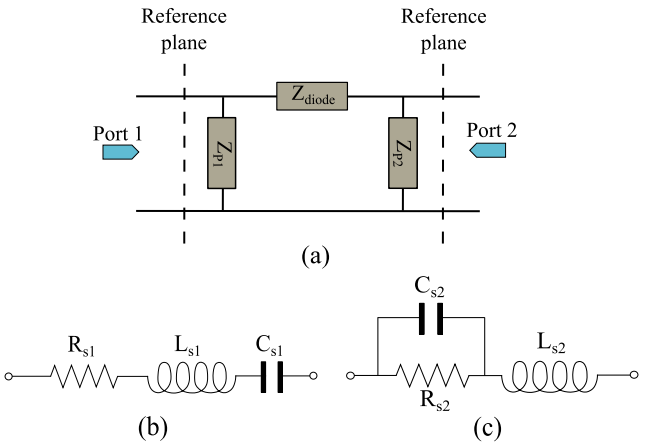

FIGURE 12. **(a) Π-equivalent model of PIN diode. Equivalent model of Z_{diode} when the DC bias current equals (b) 10 mA [ON state] and (c) 0 mA [OFF state].**

actual antenna design. The RLC network shown in Fig. 12(b) is selected to accurately model the RF behavior of the PIN diode in its ON state [10 mA], when it acts as a non-ideal short-circuit. In that case, Z_{diode} represents an RLC series network with $R_{s1} = 5.5\ \Omega$, $L_{s1} = 0.61$ nH, and $C_{s1} = 3.26$ pF. The PIN diode in the OFF state [0 mA], at a reverse voltage V_r = -1.4 V, is modeled by an inductance L_{s2} = 1.1 nH, in series with a parallel RC network with R_{s2} = 10 kΩ and C_{s2} = 35 fF [Fig. 12(c)].

B. DC POWER CONSUMPTION AND ANTENNA EFFICIENCY

In each polarization state, four out of eight PIN diodes are biased in the ON state, while the others are switched OFF, so only approximately half of them are dissipating power. Furthermore, the DC power consumption can be reduced by biasing the PIN diodes with the minimum bias current (1 mA) to polarize them in their forward state. However, when reducing the DC bias current to its minimum, the RF series resistance will increase, since the active PIN diodes act as current-controlled RF resistors. Hence, an inherent trade-off between DC power consumption and the total antenna efficiency arises. The optimal DC bias current in terms of DC power consumption and antenna radiation efficiency is found by evaluating the measured total antenna efficiency for different bias current values [see Section IV].

C. PROTOTYPE FABRICATION

A prototype of the polarization-reconfigurable probe-fed AFSIW cavity-backed slot antenna has been fabricated to validate the design. Fig. 13 depicts the fabricated antenna, whereas Fig. 14 shows a photograph of the PIN diode soldered to the antenna. In the fabrication process, a 0.25-mm-thick low-cost I-Tera MT40 substrate ($\epsilon_r = 3.43$, $\tan\delta = 0.014$ @5.5 GHz) is exploited for both Layer A and Layer C. Layer B is implemented in PLA ($\epsilon_c = 2.0$, $\tan\delta = 0.03$ @5.5 GHz) with an infill percentage of 50% by the 3D-printing fused decomposition modeling (FDM) method of the *Ultimaker* 2 [45]. All permittivity and loss tangent values of the materials are extracted by the material characterization technique described in [42]. Subsequently, Layer A and Layer C are assembled on the top and bottom of Layer B by means of flat-flange brass tubelets, spaced closely enough to minimize radiation loss. In this work, a manual tubelet press machine was used to fix the tubelets at their correct locations. For mass-production industrial applications, fully-automated tubelet machines or computer numerically controlled (CNC) tubelet-punching machines can be applied. To ensure perfect connection between the upper and lower conductive layers in Layer A and Layer C, the via holes were plated in the PCB manufacturing process.

IV. MEASUREMENT RESULTS

This section describes and analyzes the performance of the fabricated polarization reconfigurable AFSIW cavity-backed slot antenna in terms of reflection coefficient, radiation

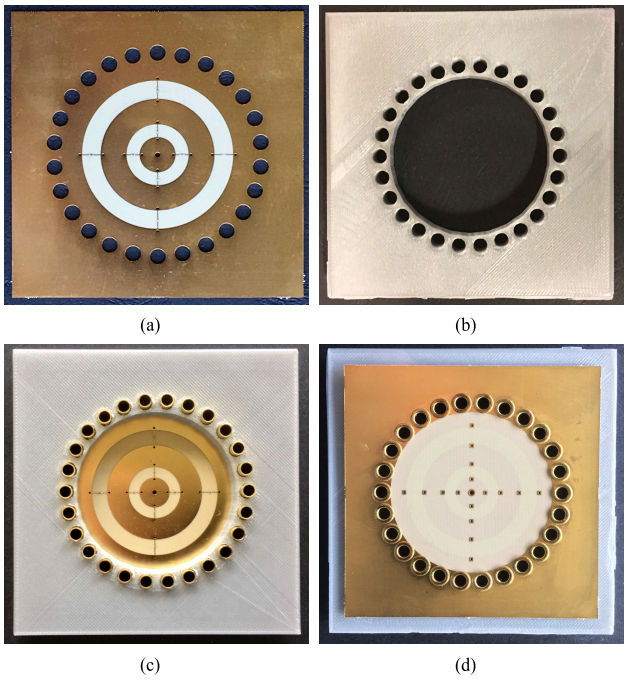

FIGURE 13. Picture of the fabricated polarization reconfigurable AFSIW cavity backed slot antenna element. (a) Back side of Layer A (after PIN diodes soldering process). (b) Layer B. (c) Back side of Layer A assembled with Layer B before adding Layer C. (d) Top view of assembled prototype.

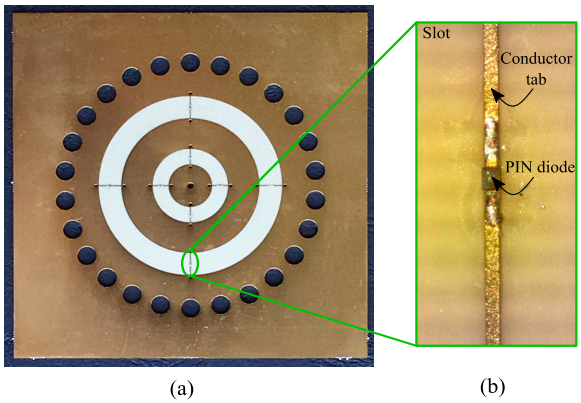

FIGURE 14. (a) Backside picture of Layer A. (b) Microscopic view of the PIN diode soldered to the antenna.

efficiency, radiation pattern, and DC power consumption. The reflection coefficients were measured with an Agilent N5242A PNA-X Microwave Network Analyzer. The radiation parameters were measured in an anechoic chamber by means of an NSI MI near-field antenna measurement system. A Keithley, 2450 sourcemeter and a Mini-Circuits, ZX85-12G-S+ bias tee were employed for DC biasing, according to Fig. 11.

The measured reflection coefficients for both polarization states are shown in Fig. 15, along with the full-wave simulation results. Owing to the geometrical and modal symmetry to the $\varphi = 0°$ and $\varphi = 90°$ planes, the orientation of the linear polarization can be changed without altering the input reflection coefficient. For both states, the fabricated antenna

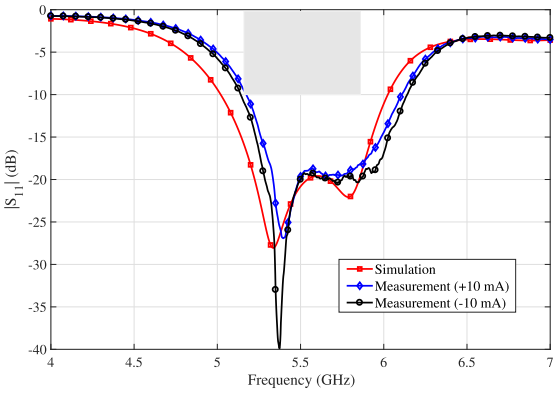

FIGURE 15. Magnitude of input reflection coefficient $|S_{11}|$ in two operating states: *y*-oriented linear polarization (bias current of +10 mA) and *x*-oriented linear polarization (bias currents of −10 mA).

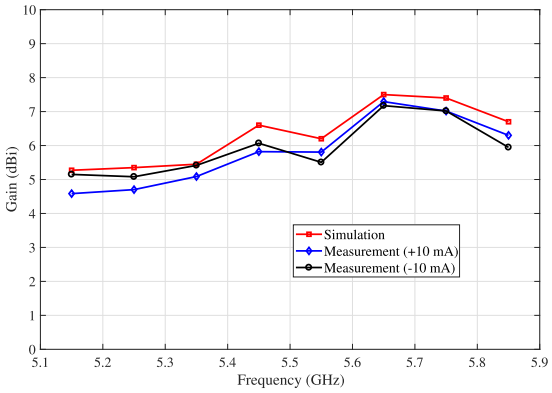

FIGURE 17. Measured and simulated maximum gain across the operating band in two polarization states: *y*-oriented linear polarization (bias current of +10 mA) and *x*-oriented linear polarization (bias current of −10 mA).

exhibits a reflection coefficient below −10 dB from 5.15 GHz to 6.08 GHz, thereby covering the entire [5.15-5.85] GHz U-NII radio communication band with and impedance bandwidth margin of 230 MHz.

Fig. 16 shows the measured DC power dissipation and total antenna efficiency as a function of the DC bias current. As seen in Fig. 16, the DC power dissipation is only 27 mW when the DC bias current is set to 10 mA. Moreover, it can be further reduced to 2.8 mW by biasing the PIN diodes with a reduced bias current of 1 mA. However, by reducing the bias current from 10 mA to 1 mA, the total antenna efficiency reduces significantly from 96 % to 63 %. In fact, this significant reduction can be attributed to a higher mismatch and lower radiation efficiency due to the higher PIN diode RF resistance at lower bias currents.

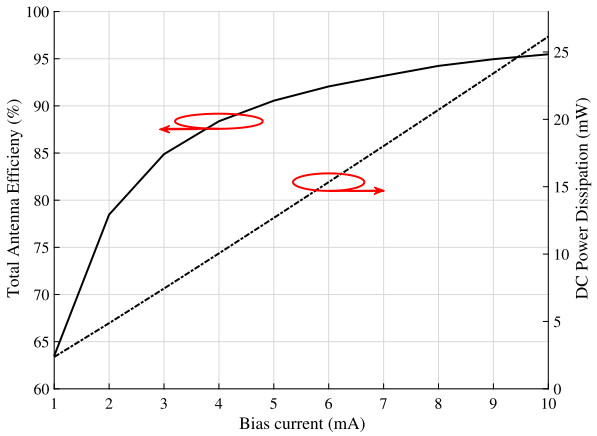

FIGURE 16. Measured total antenna efficiency at 5.6 GHz and DC power dissipation as a function of DC bias current.

The measured maximum gain values of both linear polarization states across the operating band is depicted in Fig. 17. The antenna exhibits a stable gain over the entire frequency range of operation and yields a peak gain of 7.3 dBi for both of the polarization states.

The simulated and measured radiation patterns of the antenna are compared in Fig. 18 and Fig. 19 at 5.15 GHz,

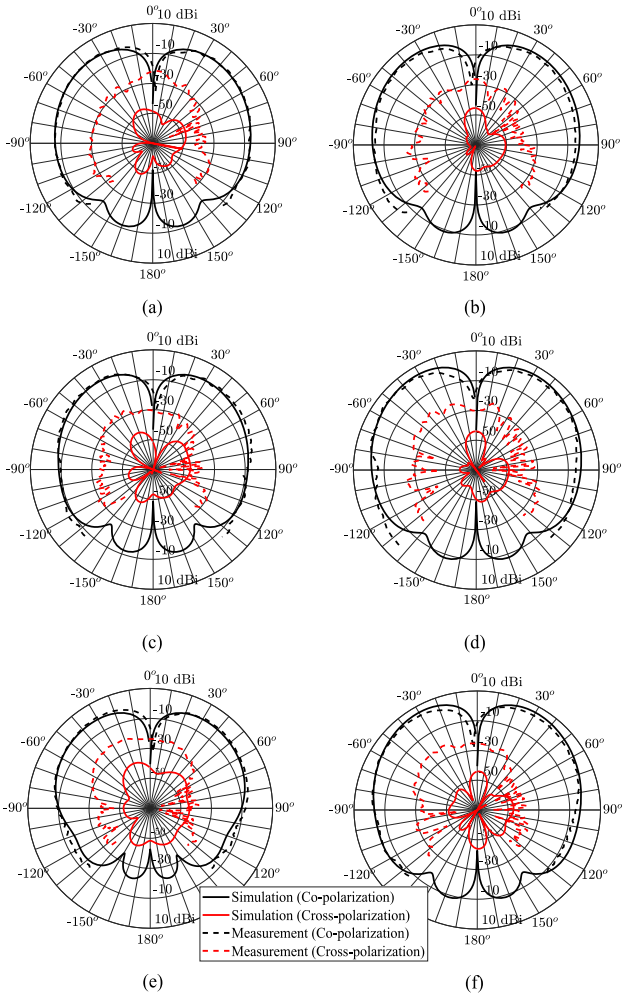

FIGURE 18. Radiation patterns at 5.15 GHz in (a) the XZ-plane and (b) the YZ-plane, at 5.50 GHz in (c) the XZ-plane and (d) the YZ-plane, at 5.85 GHz in (e) the XZ-plane and (f) the YZ-plane for the bias current set to +10 mA, meaning that the antenna exhibits *y*-oriented linear polarization.

5.5 GHz and 5.85 GHz, for a bias current of +10 mA and −10 mA, respectively. It can be seen that the simulated and measured co-polarized gain are in good agreement,

TABLE 2. Minimum measured (simulated) cross-polarization ratio (in dB) in an angular elevation sector of ±[30° - 90°].

Polarization	*Frequency (GHz)*		
	5.15	5.50	5.85
x-oriented	26.9 (49.4)	28.3 (42.4)	28.3 (42.7)
y-oriented	23.6 (48.1)	23.3 (46.8)	25.1 (43.3)

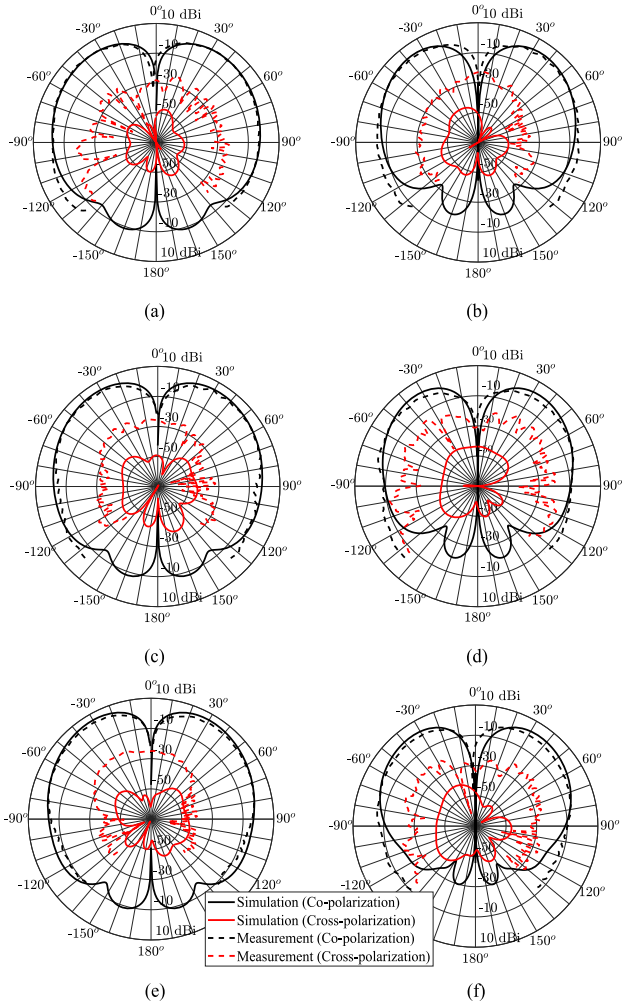

FIGURE 19. Radiation patterns at 5.15 GHz in (a) the XZ-plane and (b) the YZ-plane, at 5.50 GHz in (c) the XZ-plane and (d) the YZ-plane, at 5.85 GHz in (e) the XZ-plane and (f) the YZ-plane for the bias current set to −10 mA, meaning that the antenna exhibits *x*-oriented linear polarization.

and significantly higher than the cross-polarized gain. A measured gain of 5.8 dBi at the direction $(\theta, \varphi) = (33°, 0°)$, a 3-dB beamwidth of more than 47° and a total efficiency of 95% is obtained at 5.5 GHz for a bias current of +10 mA, meaning that the antenna exhibits y-oriented polarization. The minimum measured (simulated) cross-polarization ratio [defined as the ratio of the co-polarization gain to the cross-polarization gain] in an angular elevation sector of ±[30° - 90°] at the start, center, and end operation frequencies is summarized in Table 2. While the measured cross-polarized field turns out to be larger than simulated due to the measurement setup, the measured cross-polarization ratio still remains higher than 20 dB across the complete band of operation. The measured front-to-back ratio [defined as the ratio between maximum gain in the frontal hemisphere w.r.t. the maximum gain in the back hemisphere] is larger than 14 dB. Fig. 19 shows the radiation patterns of the antenna when the bias current is set to −10 mA, such that the antenna exhibits x-oriented polarization. Now, the maximum gain is 5.8 dBi and occurs at $(\theta, \varphi) = (33°, 90°)$. A 3 dB-beamwidth of 48° is obtained. It is found that the radiation performance of both polarization states is identical, owing to the symmetry in the antenna topology.

Table 3 compares the measured performance of our circular AFSIW cavity-backed annular slot antenna to other reported topologies. It is clear that our topology achieves a significantly larger impedance bandwidth and radiation efficiency, while maintaining a high antenna gain. The references with a higher antenna gain rely on array configurations to increase the gain in the broadside direction. Moreover, owing to its substrate-independent radiation efficiency, our antenna topology maintains stable antenna performance, even after direct implementation in everyday surfaces, in contrast to other state-of-the-art designs.

V. CONCLUSIONS

A new single-feed polarization-reconfigurable highly-efficient ultra-wideband AFSIW cavity-backed slot antenna with in-cavity electronics was proposed, fabricated and validated to meet the stringent requirements of next generation IoT applications. By exploiting 3D-printing technology, a thick antenna substrate was constructed in a cost-effective manner, while minimizing losses by introducing a well-defined air-filled region containing the electromagnetic fields. An analytical expression was derived for the effective permittivity and loss tangent of circular AFSIW antennas to provide antenna designers with a straightforward design procedure to guarantee low losses and material-independent

TABLE 3. Performance comparison of polarization-reconfigurable antennas.

Ref.	[16]	[46]	[47]	[48]	[49]	[50]	[51]	This work
Number of polarization states	3	2	6	2	4	3	3	2
Overlapped bandwidth (%)	2	3.4	1.1	4.31	1.2	0.34	3.25	16.3
Number of antenna elements	1	1	1	4	1	4	4	1
Overlapped peak gain (dBi)	3	5.7	7	11.6	4.7	10.6	10.75	7.3
Peak radiation efficiency (%)	60	-	-	55	49	-	71.6	>95
Number of ports	1	2	2	4	1	1	1	1
Antenna size (λ_0)	0.2x0.2	1x1	0.8x0.8	2.5x1.3	0.9x0.8	3.1x2.7	2.9x2.3	1.1x1.1

performance. A conical radiation pattern was generated by exciting $TE_{11,\text{slot}}$ even modes in two concentric annular slots, both split in two by shorting tabs that create a virtual electric wall. Stable and ultra-wideband impedance matching is obtained for both orthogonal polarization states without additional reconfigurable matching networks by judiciously positioning the resonance frequency of both modes in the frequency band of operation and leveraging the antenna's symmetry. This topology allows reconfiguration of the antenna polarization through a very simple, yet effective, mechanism. By electrically shorting the slots at well-defined positions by means of PIN diodes, dynamic polarization reconfiguration is obtained by changing the polarity of the DC bias current, supplied at the antenna feed by means of an external bias tee. This straightforward bias network enables the integration of all polarization control electronics inside the antenna cavity to protect them from environmental effects. Finally, measurements show that the prototype exhibits excellent performance within the entire frequency band from 5.15 GHz to 6.08 GHz band, for both polarization states.

ACKNOWLEDGMENT

The authors would like to thank the Centre for Microsystems Technology (CMST) and its expertise centre Namifab at Ghent University and in particular Dr. Björn Vandecasteele, for his skillful help during soldering of the electronic components. The authors also thank Ing. Quinten Van den Brande and Ir. Thomas Deckymn for their help in the measurements.

REFERENCES

[1] H. Sundmaeker, P. Guillemin, P. Friess, and S. Woelfflé, "Vision and challenges for realising the Internet of Things," *Eur. Commision Cluster Eur. Res. Projects Internet Things*, vol. 3, no. 3, pp. 34–36, 2010.

[2] S. Lemey, T. Castel, P. Van Torre, T. Vervust, J. Vanfleteren, P. Demeester, D. V. Ginste, and H. Rogier, "Threefold rotationally symmetric SIW antenna array for ultra-short-range MIMO communication," *IEEE Trans. Antennas Propag.*, vol. 64, no. 5, pp. 1689–1699, May 2016.

[3] C. J. Hansen, "WiGig: Multi-gigabit wireless communications in the 60 GHz band," *IEEE Wireless Commun.*, vol. 18, no. 6, pp. 6–7, Dec. 2011.

[4] N. J. McEwan, R. A. Abd-Alhameed, E. M. Ibrahim, P. S. Excell, and J. G. Gardiner, "A new design of horizontally polarizedand dual-polarized uniplanar conical beam antennas for HIPERLAN," *IEEE Trans. Antennas Propag.*, vol. 51, no. 2, pp. 229–237, Feb. 2003.

[5] Z.-C. Hao, H.-H. Wang, and W. Hong, "A novel planar reconfigurable monopulse antenna for indoor smart wireless access points' application," *IEEE Trans. Antennas Propag.*, vol. 64, no. 4, pp. 1250–1261, Apr. 2016.

[6] S. Lemey, S. Agneessens, P. Van Torre, K. Baes, J. Vanfleteren, and H. Rogier, "Wearable flexible lightweight modular RFID tag with integrated energy harvester," *IEEE Trans. Microw. Theory Techn.*, vol. 64, no. 7, pp. 2304–2314, Jul. 2016.

[7] S. Lemey, O. Caytan, D. V. Ginste, P. Demeester, H. Rogier, and M. Bozzi, "SIW cavity-backed slot (multi-)antenna systems for the next generation IoT applications," in *Proc. IEEE Top. Conf. Wireless Sensors Sensor Netw.*, Austin, TX, USA, Jan. 2016, pp. 75–77.

[8] M. Bozzi, S. Moscato, L. Silvestri, N. Delmonte, M. Pasian, and L. Perregrini, "Innovative SIW components on paper, textile, and 3D-printed substrates for the Internet of Things," in *Proc. Asia–Pacific Microw. Conf.*, Nanjing, China, Dec. 2015, pp. 1–3.

[9] W. Lin and H. Wong, "Multipolarization-reconfigurable circular patch antenna with L-shaped probes," *IEEE Antennas Wireless Propag. Lett.*, vol. 16, pp. 1549–1552, 2017.

[10] W. Lin and H. Wong, "Wideband circular-polarization reconfigurable antenna with L-shaped feeding probes," *IEEE Antennas Wireless Propag. Lett.*, vol. 16, pp. 2114–2117, 2017.

[11] Y. J. Guo, P.-Y. Qin, S.-L. Chen, W. Lin, and R. W. Ziolkowski, "Advances in reconfigurable antenna systems facilitated by innovative technologies," *IEEE Access*, vol. 6, pp. 5780–5794, Jan. 2018.

[12] L.-Y. Ji, P.-Y. Qin, Y. J. Guo, C. Ding, G. Fu, and S.-X. Gong, "A wideband polarization reconfigurable antenna with partially reflective surface," *IEEE Trans. Antenna Propag.*, vol. 64, no. 10, pp. 4534–4538, Oct. 2016.

[13] J.-S. Row and C.-J. Shih, "Polarization-diversity ring slot antenna with frequency agility," *IEEE Trans. Antennas Propag.*, vol. 60, no. 8, pp. 3953–3957, Aug. 2012.

[14] J.-S. Row and Y.-H. Wei, "Wideband reconfigurable crossed-dipole antenna with quad-polarization diversity," *IEEE Trans. Antennas Propag.*, vol. 66, no. 4, pp. 2090–2094, Apr. 2018.

[15] H. Sun and S. Sun, "A novel reconfigurable feeding network for quad-polarization-agile antenna design," *IEEE Trans. Antenna Propag.*, vol. 64, no. 1, pp. 311–316, Jan. 2016.

[16] N. Nguyen-Trong, A. Piotrowski, L. Hall, and C. Fumeaux, "A frequency- and polarization-reconfigurable circular cavity antenna," *IEEE Antennas Wireless Propag. Lett.*, vol. 16, pp. 999–1002, 2017.

[17] P.-Y. Qin, A. R. Weily, Y. J. Guo, and C.-H. Liang, "Polarization reconfigurable U-slot patch antenna," *IEEE Trans. Antennas Propag.*, vol. 58, no. 10, pp. 3383–3388, Oct. 2010.

[18] M. S. Nishamol, V. P. Sarin, D. Tony, C. K. Aanandan, P. Mohanan, and K. Vasudevan, "An electronically reconfigurable microstrip antenna with switchable slots for polarization diversity," *IEEE Trans. Antenna Propag.*, vol. 59, no. 9, pp. 3424–3427, Sep. 2011.

[19] T. Song, Y. Lee, D. Ga, and J. Choi, "A polarization reconfigurable microstrip patch antenna using PIN diodes," in *Proc. Asia–Pacific Microw. Conf.*, Kaohsiung, Taiwan, Dec. 2012, pp. 616–618.

[20] A. Khidre, K.-F. Lee, F. Yang, and A. Z. Elsherbeni, "Circular polarization reconfigurable wideband E-shaped patch antenna for wireless applications," *IEEE Trans. Antennas Propag.*, vol. 61, no. 2, pp. 960–964, Feb. 2013.

[21] S. Nikolaou, R. Bairavasubramanian, C. Lugo, I. Carrasquillo, D. C. Thompson, G. E. Ponchak, J. Papapolymerou, and M. M. Tentzeris, "Pattern and frequency reconfigurable annular slot antenna using PIN diodes," *IEEE Trans. Antennas Propag.*, vol. 54, no. 2, pp. 439–448, Feb. 2006.

[22] W. Lin and H. Wong, "Polarization reconfigurable wheel-shaped antenna with conical-beam radiation pattern," *IEEE Trans. Antennas Propag.*, vol. 63, no. 2, pp. 491–499, Feb. 2015.

[23] G. Q. Luo, T. Y. Wang, and X. H. Zhang, "Review of low profile substrate integrated waveguide cavity backed antennas," *Int. J. Antennas Propag.*, vol. 2013, Oct. 2013, Art. no. 746920.

[24] M. Bozzi, A. Georgiadis, and K. Wu, "Review of substrate-integrated waveguide circuits and antennas," *IET Microw. Antennas Propag.*, vol. 5, no. 8, pp. 909–920, Jun. 2011.

[25] Z. Li and K. Wu, "24-GHz frequency-modulation continuous-wave radar front-end system-on-substrate," *IEEE Trans. Microw. Theory Techn.*, vol. 56, no. 2, pp. 278–285, Feb. 2008.

[26] Q. Van den Brande, S. Lemey, J. Vanfleteren, and H. Rogier, "Highly efficient impulse-radio ultra-wideband cavity-backed slot antenna in stacked air-filled substrate integrated waveguide technology," *IEEE Trans. Antennas Propag.*, vol. 66, no. 5, pp. 2199–2209, May 2018.

[27] Y. Cai, Y. Zhang, C. Ding, and Z. Qian, "A wideband multilayer substrate integrated waveguide cavity-backed slot antenna array," *IEEE Trans. Antenna Propag.*, vol. 65, no. 7, pp. 3465–3473, Jul. 2017.

[28] S. Moscato, R. Moro, M. Pasian, M. Bozzi, and L. Perregrini, "Innovative manufacturing approach for paper-based substrate integrated waveguide components and antennas," *IET Microw., Antennas Propag.*, vol. 10, no. 3, pp. 256–263, 2016.

[29] R. Moro, S. Agneessens, H. Rogier, A. Dierck, and M. Bozzi, "Textile microwave components in substrate integrated waveguide technology," *IEEE Trans. Microw. Theory Techn.*, vol. 63, no. 2, pp. 422–432, Feb. 2015.

[30] R. Moro, M. Bozzi, A. Collado, A. Georgiadis, and S. Via, "Plastic-based substrate integrated waveguide (SIW) components and antennas," in *Proc. Eur. Microw. Conf.*, Amsterdam, The Netherlands, Oct./Nov. 2012, pp. 1007–1010.
[31] K. Y. Kapusuz, S. Lemey, and H. Rogier, "Substrate-independent microwave components in substrate integrated waveguide technology for high-performance smart surfaces," *IEEE Trans. Microw. Theory Techn.*, vol. 66, no. 6, pp. 3036–3047, Jun. 2018.
[32] "Revision of part 15 of the commission's rules regarding ultra-wideband transmission systems," Federal Commun. Commission, Washington, DC, USA, Tech. Rep. ET Docket 98-153, Apr. 2002.
[33] S. Moscato, R. Bahr, T. Le, M. Pasian, M. Bozzi, L. Perregrini, and M. M. Tentzeris, "Infill-dependent 3-D-printed material based on ninjaflex filament for antenna applications," *IEEE Antennas Wireless Propag. Lett.*, vol. 15, pp. 1506–1509, 2016.
[34] S. Moscato, R. Bahr, T. Le, M. Pasian, M. Bozzi, L. Perregrini, and M. M. Tentzeris, "Additive manufacturing of 3D substrate integrated waveguide components," *Electron. Lett.*, vol. 51, no. 18, pp. 1426–1428, Mar. 2015.
[35] E. Massoni, L. Silvestri, G. Alaimo, S. Marconi, M. Bozzi, L. Perregrini, and F. Auricchio, "3-D printed substrate integrated slab waveguide for single-mode bandwidth enhancement," *IEEE Microw. Wireless Compon. Lett.*, vol. 27, no. 6, pp. 536–538, Jun. 2017.
[36] D.-F. Guan, Z.-P. Qian, W.-Q. Cao, L.-Y. Ji, and Y.-S. Zhang, "Compact SIW annular ring slot antenna with multiband multimode characteristics," *IEEE Trans. Antennas Propag.*, vol. 63, no. 12, pp. 5918–5922, Dec. 2015.
[37] J.-S. Chen, "Dual-frequency annular-ring slot antennas fed by CPW feed and microstrip line feed," *IEEE Trans. Antennas Propag.*, vol. 53, no. 1, pp. 569–573, Jan. 2005.
[38] G. Q. Luo, Z. F. Hu, L. X. Dong, and L. L. Sun, "Planar slot antenna backed by substrate integrated waveguide cavity," *IEEE Antennas Wireless Propag. Lett.*, vol. 7, pp. 236–239, Apr. 2008.
[39] J. R. James and P. Hall, Eds., *Handbook of Microstrip Antennas*, vol. 1. Edison, NJ, USA: IET, 1989, ch. 3, pp. 111–217.
[40] P. Bienstman, H. Derudder, R. Baets, F. Olyslager, and D. D. Zutter, "Analysis of cylindrical waveguide discontinuities using vectorial eigenmodes and perfectly matched layers," *IEEE Trans. Microw. Theory Techn.*, vol. 49, no. 2, pp. 349–354, Feb. 2001.
[41] Q. Tan, Y. Guo, L. Zhang, F. Lu, H. Dong, and J. Xiong, "Substrate integrated waveguide (SIW)-based wireless temperature sensor for harsh environments," *Sensors*, vol. 18, no. 5, p. 1406, May 2018.
[42] F. Declercq, H. Rogier, and C. Hertleer, "Permittivity and loss tangent characterization for garment antennas based on a new matrix-pencil two-line method," *IEEE Trans. Antennas Propag.*, vol. 56, no. 8, pp. 2548–2554, Aug. 2008.
[43] G. Q. Luo, Z. F. Hu, W. J. Li, X. H. Zhang, L. L. Sun, and J. F. Zheng, "Bandwidth-enhanced low-profile cavity-backed slot antenna by using hybrid SIW cavity modes," *IEEE Trans. Antennas Propag.*, vol. 60, no. 4, pp. 1698–1704, Apr. 2012.
[44] M. Yousefbeiki and J. Perruisseau-Carrier, "A practical technique for accurately modeling reconfigurable lumped components in commercial full-wave solvers," *IEEE Antennas Propag. Mag.*, vol. 54, no. 5, pp. 298–303, Oct. 2012.
[45] *Ultimaker*. Accessed: Jul. 12, 2019. [Online]. Available: https://ultimaker.com/
[46] A. Kumar and S. Raghavan, "Broadband dual-circularly polarised SIW cavity antenna using a stacked structure," *Electron. Lett.*, vol. 53, no. 17, pp. 1171–1172, Sep. 2017.
[47] H. Lee, Y. Sung, C. T. M. Wu, and T. Itoh, "Dual-band and polarization-flexible cavity antenna based on substrate integrated waveguide," *IEEE Antennas Wireless Propag. Lett.*, vol. 15, pp. 488–491, 2016.
[48] P. Vasina, T. Mikulasek, J. Lacik, and H. Arthaber, "Beam- and polarisation-reconfigurable SIW ring-slot antenna array," *IET Microw., Antennas Propag.*, vol. 12, no. 15, pp. 2313–2319, Oct. 2018.
[49] L. Ge, Y. Li, J. Wang, and C.-Y.-D. Sim, "A low-profile reconfigurable cavity-backed slot antenna with frequency, polarization, and radiation pattern agility," *IEEE Trans. Antenna Propag.*, vol. 65, no. 5, pp. 2182–2189, May 2017.
[50] Z.-C. Hao, K.-K. Fan, and H. Wang, "A planar polarization-reconfigurable antenna," *IEEE Trans. Antennas Propag.*, vol. 65, no. 4, pp. 1624–1632, Apr. 2017.
[51] J. Hu, Z. C. Hao, and Z. W. Miao, "Design and implementation of a planar polarization-reconfigurable antenna," *IEEE Antennas Wireless Propag. Lett.*, vol. 16, pp. 1557–1560, 2017.

KAMIL YAVUZ KAPUSUZ (S'17) was born in 1988. He received the M.Sc. degree in electrical engineering from Atilim University, Ankara, Turkey, in 2013. He is currently pursuing the Ph.D. degree in electrical engineering with the Electromagnetics Group, Department of Information Technology, Ghent, Belgium.

From 2014 to 2016, he was with Remote Sensing Technologies, Ankara. He developed antenna arrays at millimeter-wave frequencies for radar applications. He also developed scalable phased array antennas for SATCOM-on-the-move concepts. His research interests include design and development of passive RF components, multifunction and reconfigurable antennas, active antenna systems, and phased arrays.

SAM LEMEY (S'14–M'16) received the M.Sc. degree in electronic engineering from Howest, University College West Flanders, Kortrijk, Belgium, in 2012, and the Ph.D. degree in electrical engineering from Ghent University, Ghent, Belgium, in 2016.

In 2018, he was a Visiting Scientist with the Terahertz Photonics Group, Institute of Electronics, Microelectronics and Nanotechnology (IEMN), University Lille Nord de France, Lille, France. He is currently an Assistant Professor with Ghent University and a Postdoctoral Fellow of the Special Research Fund (BOF), affiliated with the IDLab, Electromagnetics Group, Department of Information Technology (INTEC), Ghent University/imec. His research interests include robust antenna systems for wearable applications, antennas on unconventional substrates, active antenna design for the Internet of Things and 5G applications, (opto-electronic) millimeter-wave and terahertz multi-antenna systems, impulse-radio ultra-wideband antenna systems for centimeter-precision localization, and full-wave/circuit co-optimization frameworks to realize (opto-electronic) active (multi-)antenna systems.

Dr. Lemey received the Best Paper Award at the 2016 IEEE MTT-S Topical Conference on Wireless Sensors and Sensor Networks.

ALESSANDRA PETROCCHI was born in San Severino Marche, Italy, in 1989. She received the M.S. degree in engineering for telecommunications and electronics from the University of Ferrara, Ferrara, Italy, in 2015. She is currently pursuing the joint Ph.D. degree in electrical engineering with KU Leuven, Leuven, Belgium, and the University of Ferrara. Since 2015, she has been with the Department of Electrical Engineering (ESAT), Leuven. Her research interest includes the design a radio-frequency front-end for the Internet-of-Things application.

PIET DEMEESTER (M'86–F'08) received the M.Sc. and Ph.D. degrees in electrical engineering from Ghent University, Ghent, Belgium, in 1984 and 1988, respectively.

He is currently a Professor with Ghent University and the Director of the IDLab, imec. He is a coauthor of over 1000 international publications and a holder of an advanced ERC grant. His research interests include artificial intelligence for the IoT and robotics, machine learning and data mining, semantic intelligence, cloud and big data infrastructures, fixed networking, wireless networking, electromagnetics, and high-frequency design.

DOMINIQUE SCHREURS (S'90–M'97–SM'02–F'12) received the M.Sc. degree in electronic engineering and the Ph.D. degree from the University of Leuven (KU Leuven), Leuven, Belgium.

She has been a Visiting Scientist with Agilent Technologies, Santa Rosa, CA, USA, ETH Zurich, Zürich, Switzerland, and the National Institute of Standards and Technology, Boulder, CO, USA. She is currently a Full Professor with KU Leuven, where she is also the Chair of the Leuven LICT. Her current research interests include the microwave and millimeter-wave characterization and modeling of transistors, nonlinear circuits, and bioliquids, and system design for wireless communications and biomedical applications.

Dr. Schreurs was an IEEE MTT-S Distinguished Microwave Lecturer. She is also the President of the IEEE Microwave Theory and Techniques Society. She was the General Chair of the 2007, 2012, and 2018 Spring ARFTG Conferences. She is currently the President of the ARFTG Organization. She was the Editor-in-Chief of the IEEE TRANSACTIONS ON MICROWAVE THEORY AND TECHNIQUES.

HENDRIK ROGIER (SM'06) received the M.Sc. and Ph.D. degrees in electrical engineering from Ghent University, Ghent, Belgium, in 1994 and 1999, respectively.

From 2003 to 2004, he was a Visiting Scientist with the Mobile Communications Group, Vienna University of Technology, Vienna, Austria. He is a currently a Full Professor with the Department of Information Technology, Ghent University, a Guest Professor with the Interuniversity Microelectronics Centre, Ghent, and a Visiting Professor with the University of Buckingham, Buckingham, U.K. He has authored or coauthored over 160 papers in international journals and over 180 contributions in conference proceedings. His current research interests include antenna systems, radio wave propagation, body-centric communication, numerical electromagnetics, electromagnetic compatibility, and power/signal integrity.

Dr. Rogier is a member of the Technical Committee 24 on RFID Technology of the IEEE Microwave Theory and Techniques Society (MTT-S) and a member of the Governing Board of the Topical Group MAGEO on Microwaves in Agriculture, Environment, and Earth Observation of the European Microwave Association, Leuven, Belgium. He was a recipient of the URSI Young Scientist Award (twice) at the 2001 URSI Symposium on Electromagnetic Theory and the 2002 URSI General Assembly, the Best Poster Paper Award at the 2012 IEEE Electrical Design of Advanced Packaging and Systems Symposium, the Best Paper Award at the 2013 IEEE Workshop on Signal and Power Integrity, the Joseph Morrissey Memorial Award for the First Best Scientific Paper at BioEM 2013, the 2014 Premium Award for Best Paper of *IET Electronics Letters*, and the Best Paper Award First Place at the 2016 IEEE MTT-S Topical Conference on Wireless Sensors and Sensor Networks. He is also an Associate Editor of *IET Electronics Letters*, *IET Microwaves, Antennas, and Propagation*, and the IEEE TRANSACTIONS ON MICROWAVE THEORY AND TECHNIQUES. He acts as the URSI Commission B Representative for Belgium.